JACS
JOURNAL OF THE AMERICAN CHEMICAL SOCIETY
pubs.acs.org/JACS
Article

Distance Dependence of Förster Resonance Energy Transfer Rates in 2D Perovskite Quantum Wells via Control of Organic Spacer Length

Shobhana Panuganti, Lucas V. Besteiro, Eugenia S. Vasileiadou, Justin M. Hoffman, Alexander O. Govorov, Stephen K. Gray, Mercouri G. Kanatzidis,* and Richard D. Schaller*

Cite This: https://dx.doi.org/10.1021/jacs.0c12441
Read Online
ACCESS | Metrics & More | Article Recommendations | Supporting Information

ABSTRACT: Two-dimensional (2D) semiconductors are attractive candidates for a variety of optoelectronic applications owing to the unique electronic properties that arise from quantum confinement along a single dimension. Incorporating nonradiative mechanisms that enable directed migration of bound charge carriers, such as Förster resonance energy transfer (FRET), could boost device efficiencies provided that FRET rates outpace undesired relaxation pathways. However, predictive models for FRET between distinct 2D states are lacking, particularly with respect to the distance d between a donor and acceptor. We approach FRET in systems with binary mixtures of donor and acceptor 2D perovskite quantum wells (PQWs), and we synthetically tune distances between donor and acceptor by varying alkylammonium spacer cation lengths. FRET rates are monitored using transient absorption spectroscopy and ultrafast photoluminescence, revealing rapid picosecond lifetimes that scale with spacer cation length. We theoretically model these binary mixtures of PQWs, describing the emitters as classical oscillating dipoles. We find agreement with our empirical lifetimes and then determine the effects of lateral extent and layer thickness, establishing fundamental principles for FRET in 2D materials.

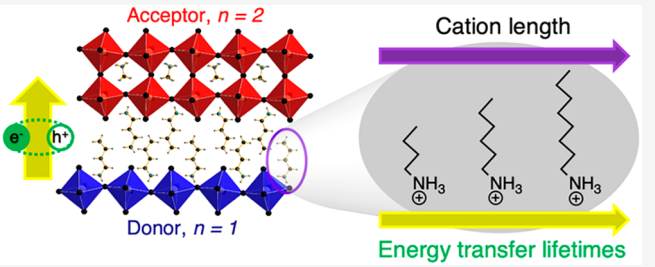

INTRODUCTION

Two-dimensional (2D) semiconductors offer prospective benefits for optoelectronics devices spanning photovoltaics, lasers, and light-emitting diodes[1−7] due to tunable quantum and dielectric confinement effects that facilitate control of electronic band gap and often give rise to strong band-edge absorption in addition to spectrally narrow photoluminescence.[8,9] However, 2D materials also typically exhibit large exciton binding energies, anisotropic conductivity, and low carrier mobilities, which can impede energy and carrier migration compared to bulk phases. Förster resonance energy transfer (FRET) offers the prospect of rapid exciton migration in 2D materials that can potentially outpace other undesirable excited-state relaxation channels such as carrier trapping, recombination, and even Auger recombination.[10,11] Fast FRET presents an opportunity to bolster the utility of 2D materials, offering routes to defect-tolerant devices and enabling novel energy-funneling architectures.[12−15]

The probability of FRET occurring between an excited donor and ground-state acceptor depends on the spectral overlap integral and electronic coupling, affected by donor−acceptor distance d, between states.[16] However, Förster theory models donor and acceptor states as point dipoles, and while appropriate for molecular and quantum dot (QD) systems, it cannot describe energy transfer between states with a 2D spatial extent (see Figure 1a). The generalization of Förster theory to higher dimension structures requires an empirical investigation to guide and test models.[17,18] Experimental studies of FRET in 2D systems, such as colloidal nanoplatelets, graphene, and transition metal dichalcogenides, have indicated rapid lifetimes on hundreds to few picosecond time scales.[19−28]

To this end, 2D perovskite quantum wells (PQWs) with mixtures of different n thicknesses and, therefore, different energy gaps present promising experimental systems for studies of Förster theory in 2D systems. PQWs form upon the incorporation of large, organic cations into the bulk hybrid perovskite framework, which introduces low-dielectric organic barriers between layers of PQWs.[29] The resulting materials are composed of precisely n octahedra in each PQW along the stacking axis and exhibit the general formula $A'_2A_{n-1}M_nX_{3n+1}$ where A′ is the larger "spacer" cation constituting the organic barrier, A is the small organic cation occupying the perovskite cage, M is the divalent metal, and X is the halide.

At present, reports focused on 2D PQWs offer disparities regarding FRET rates, though examined sample structures and

Received: November 29, 2020

https://dx.doi.org/10.1021/jacs.0c12441
J. Am. Chem. Soc. XXXX, XXX, XXX−XXX

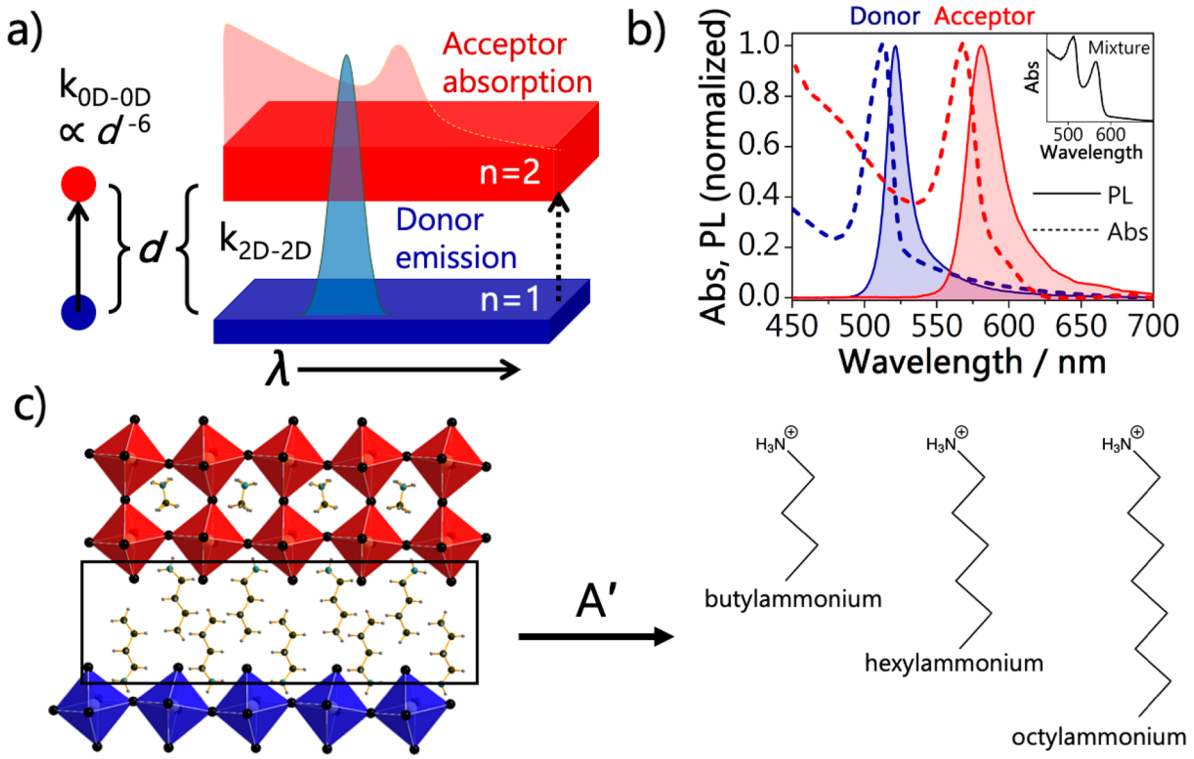

Figure 1. Static characterization of 2D PQWs. (a) Förster theory describes energy transfer between point dipoles with FRET rates (k_{0D-0D}) scaling with the distance (d) between the donor and acceptor. The 2D spatial extent of 2D PQWs with requisite spectral overlap is hypothesized to increase FRET rates (k_{2D-2D}) owing to the increased effective density of the acceptor, but quantitative theoretical and empirical models have not been developed. (b) Absorption and photoluminescence spectra of donor (n = 1) and acceptor (n = 2) phases of $(BA)_2MA_{n-1}Pb_nI_{3n+1}$. (c) Structural visualization of a donor and acceptor interface in a binary mixture showing layers of $[PbI_6]^{4-}$ octahedra where n = 1 (blue) and n = 2 (red) are separated by the A′ site cation. Molecular structures of the A′ cations used in this study to change the distance of separation between layers are shown on the left.

mixture identities vary among these studies.[30−33] One report, which examined a broad distribution of n thickness PQWs that inclusively spanned n = 2 to n = 6, reported femtosecond FRET time scales between different n layers.[31] Other recent studies of 2D PQWs containing different A′ cations and ranges of n thickness observed remarkably longer hundred-picosecond time scales.[32,33] The results in each of these reports encounter complications arising from multiple undefined pairings of donor and acceptor species, overlapping spectral signatures that inhibit distinctly correlated dynamics of donor energy outflow with acceptor inflow, and the absence of isolated n samples. To advance the understanding of spatial dimensionality effects on rates of FRET in 2D PQWs and in materials of varying dimensionality generally, studies of energy transfer rates with individually resolved donor and acceptor dynamics in binary donor−acceptor mixtures are crucial.[34,35] Despite rapid progress in device fabrication and performance, synthetic methods for 2D PQW films containing a single n domain and controlled mixtures of n phases are underdeveloped, in particular for materials over a range of A′ cations that would enable one to study energy transfer as a function of distance between layers of 2D PQWs.[33,36,37]

In this study, we develop synthetic procedures to achieve both neat and binary mixed films comprising n = 1 and n = 2 alkylammonium lead halide 2D PQWs and probe energy transfer rates with ultrafast spectroscopy. Femtosecond transient absorption reveals correlated donor and acceptor dynamics that indicate FRET. Time-resolved photoluminescence studies are also performed, suggesting an absence of measurable charge transfer and further supporting energy transfer. We then probe FRET as a function of distance between donor and acceptor PQWs through systematic increases in carbon chain length of A′ site alkylammonium cations. The interlayer spacing between PQWs is directly affected by the steric properties of the organic cation in the A′ site (see Figure 1c); in our approach, we exploit this inherent structural feature to precisely tune the distance between layers, in particular employing butylammonium (BA), hexylammonium (HA), and octylammonium (OA) with A site methylammonium (MA) cation for n = 2 phases. Next, we construct a theoretical model of these systems and obtain results consistent with our experimental findings, observing rapid picosecond lifetimes that outpace earlier reports of Auger recombination in these materials.[38,39] We model other synthetically adjustable parameters of 2D materials, gathering results that suggest FRET lifetimes show little dependence on the isolated tuning of the lateral extent and thickness of the quantum wells. Thus, our work herein begins to build the necessary foundation for predictive models of FRET in 2D PQWs and further guides design principles for employing FRET in devices fabricated from 2D materials.

RESULTS AND DISCUSSION

Crystalline samples of phase-pure n = 1 and n = 2 $(BA)_2MA_{n-1}Pb_nI_{3n+1}$, $(HA)_2MA_{n-1}Pb_nI_{3n+1}$, and $(OA)_2MA_{n-1}Pb_nI_{3n+1}$ were synthesized according to previously published methods.[40,41] Briefly, lead oxide was dissolved into hydroiodic acid and heated to boiling while stirring to afford a

https://dx.doi.org/10.1021/jacs.0c12441
J. Am. Chem. Soc. XXXX, XXX, XXX−XXX

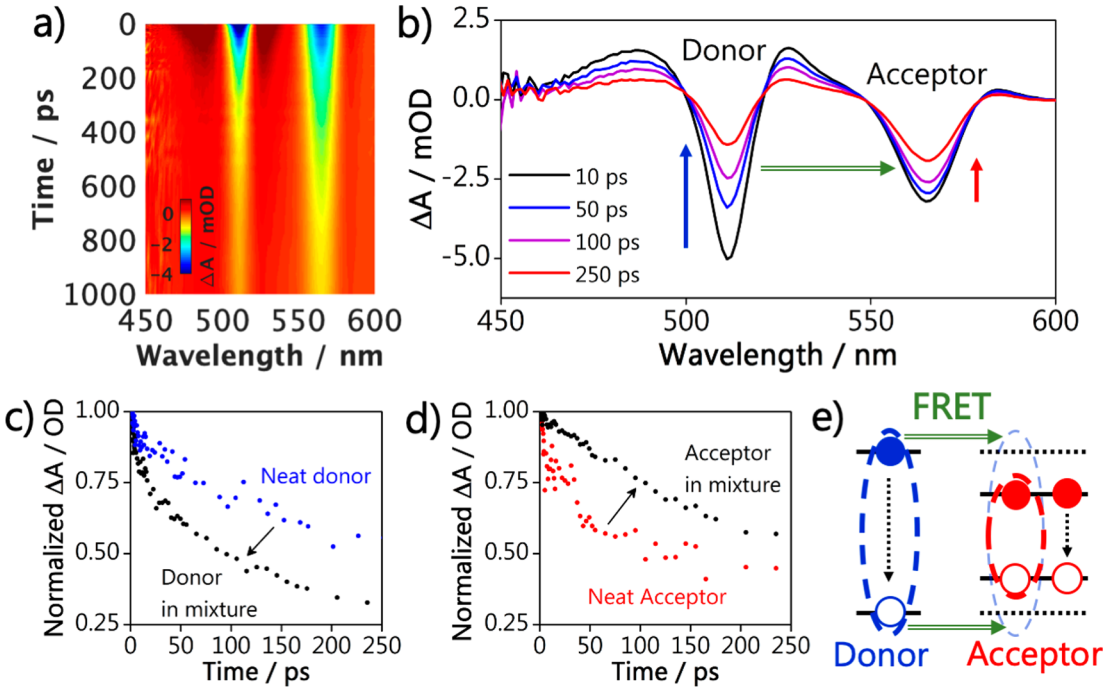

Figure 2. Dynamic optical measurements of BA $n = 1$ and $n = 2$ phase-pure and mixed composition films by transient absorption. (a) Time-resolved absorption spectral map as a function of probe wavelength showing strong negative ΔA signals upon excitation at 512 and 565 nm, which are the main absorption lines of the donor and acceptor components, respectively. Spectra shown are the average of three scans. (b) Transient absorption spectra of the mixed film at 10, 50, 100, and 250 ps with the ground-state bleach signal of the donor decaying much more rapidly compared to the acceptor. (c) Normalized decay dynamics at 496 nm from neat $n = 1$ and the mixture for the donor. (d) Normalized decay dynamics at 565 nm from neat $n = 2$ and the mixture for the acceptor. (e) Upon 400 nm excitation, both donor (blue) and acceptor (red) components in the mixture generate excitons, resulting in "bleaching" or a negative ΔA signal, of ground-state transitions. In the mixture, the donor exciton population rapidly decreases as excitons isoenergetically transfer into the acceptor, resulting in a faster decay of the donor in the mixture than the neat donor (c). The energy transfer also increases exciton population in the acceptor after excitation, resulting in a slower decay of the acceptor in the mixture than the neat acceptor (d).

bright yellow solution. Hypophosphorous acid and the appropriate ratio of alkylamine and methylammonium chloride necessary to produce the desired n phases ($n = 1, 2$) were then added to the reaction mixture. Large flake-like crystals, precipitated upon cooling, were vacuum filtered, washed with diethyl ether, and stored in an evacuated desiccator. Powder X-ray diffraction (Figure S1) of the crystalline materials compared with calculated patterns indicated phase-pure products, showing characteristic peaks in both $n = 1$ and $n = 2$.

These phase-pure crystals were then used as precursors for the preparation of both neat and binary films to obtain control over donor and acceptor density in film mixtures as well as to preclude formation of $n = 3$ or thicker PQWs. Binary films were produced by dissolving both $n = 1$ and $n = 2$ crystals into dimethylformamide (DMF) in a nitrogen atmosphere and spin-coating at 4000 rpm for 30 s onto clean, preheated (110 °C) glass substrates. Figure 1b shows absorption and photoluminescence spectra of the neat BA $n = 1$ donor and $n = 2$ acceptor films with notable spectral overlap of donor emission and acceptor absorption.

Several routes to binary films were examined, and our preferred method of film preparation was adapted from previously reported hot-casting methods in which substrates are preheated before spin-coating to produce well-oriented, homogeneous materials on the substrate surface.[2] The utilization of higher concentrations of $n = 1$, in which methylammonium is not present, was expected to inhibit the growth of higher n domains by limiting the amount of methylammonium available for thicker PQW growth. The higher relative ratio of $n = 1$ to $n = 2$ yields a donor-saturated system and a lower limit of FRET rates for the system wherein donors tend to experience a single adjacent acceptor. Importantly, mixtures of $n = 1$ and $n = 2$ PQWs retained distinct spectral features of the donor and acceptor (Figure 1b, inset). Furthermore, binary film absorption spectra conveyed the absence of secondary phases such as higher n PQWs, which would appear at redder wavelengths. Powder X-ray diffraction patterns of the binary BA films correspondingly indicated only the presence of $n = 1$ and $n = 2$ phases (Figure S2). Structural and optical characterization of HA and OA films are included in the Supporting Information.

Next, we performed femtosecond transient absorption (TA) spectroscopy using 35 fs laser pulses for both single-component films of donor or acceptor as well as binary films. TA facilitates the observation of any especially rapid processes that relate donor population outflow to acceptor inflow. In these studies, we implemented low-fluence (2.13 μJ/cm^2) excitation to avoid multiexcitonic processes that can complicate analysis as they potentially could occur on similar time scales as FRET. Figure 2a shows time-resolved changes in absorption (ΔA) signals as a function of probe wavelength for a binary BA film (neat BA films are shown in Figure S5). Above-band gap excitation at 400 nm results in "bleaching" of ground-state populations in both $n = 1$ and $n = 2$, seen as negative ΔA signals in Figure 2a,b at 513 and 565 nm, respectively. In addition, induced absorption signals appear at a higher energy of each bleach. Owing to the concern that broad $n = 2$ induced absorption signals overlap with the $n = 1$ bleach,

https://dx.doi.org/10.1021/jacs.0c12441
J. Am. Chem. Soc. XXXX, XXX, XXX−XXX

here, we analyze $n = 1$ at the induced absorption feature at 496 nm. Kinetics data in Figure 2c,d monitored at 496 and 565 nm are shown normalized at 1 ps following intraband relaxation of carriers and other convoluting processes such as optical Stark shifts.[42]

Donor transient optical signals clearly decay more rapidly in the binary mixture relative to the neat film (Figure 2c). In addition, acceptor kinetics monitored at the 565 nm ground-state bleach feature show notably slower decay signals consistent with FRET for the acceptor PQWs in the mixture relative to the neat $n = 2$ film (Figure 2d). These observations of shorter donor lifetime and correlated extended acceptor lifetime in the binary mixed film, as compared to the neat materials, convey exciton population transfer from donor to acceptor states via FRET. Importantly, rates of excited-state decay for $n = 2$ acceptors were also obtained using 545 nm excitation, as opposed to 400 nm, to selectively excite acceptors in the binary films as a means to control for potentially consequential environmental or material-processing influences relative to the neat $n = 2$ acceptor films. 545 nm is below the energy gap for $n = 1$ and was verified to not excite $n = 1$ in the neat donor films, thus allowing us to examine $n = 2$ dynamics.

Rates of FRET were obtained by differencing the normalized neat donor and acceptor decay dynamics from the corresponding measurements performed for binary mixed films. By differencing the neat film dynamics from mixed film dynamics for each n phase, we account for intrinsic electronic processes of the individual n phase in the absence of other phases and isolate the emergent energy transfer dynamics. Figure 3a shows the isolated rise in the acceptor and decay in the donor for the BA spacer with a time constant of 14 ± 2 ps. Such correlated dynamics are consistent with the conclusion that rapid FRET occurs in these films and is competitive with other nonradiative pathways that could otherwise quench donor states. However, correlated transient absorption dynamics can also occur for other charge carrier migration pathways, such as electron transfer. To determine whether a contribution from charge transfer is operative, we performed time-resolved photoluminescence measurements. Unlike charge transfer, FRET results in the migration of the entire exciton from the donor into the acceptor state (see Figure 2e) and can induce sensitized acceptor emission to which time-resolved photoluminescence is sensitive, whereas charge transfer at low excitation fluence quenches emission. Figure S6 shows representative time-resolved photoluminescence and a dynamic response from both mixed and neat OA films. This data again exhibits correlated donor decay and acceptor rise dynamics, supporting FRET and not charge transfer, on similar time scales as noted in transient absorption.

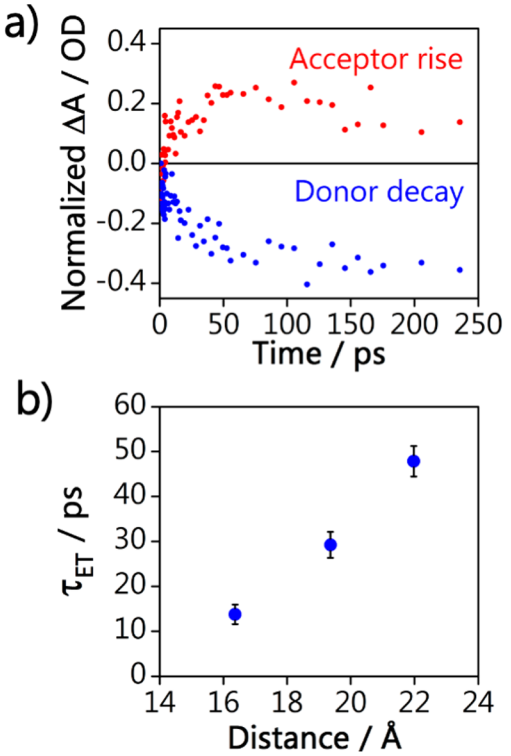

Figure 3. Energy transfer in mixed films. (a) Isolated decay in $n = 1$ donor and rise in $n = 2$ acceptor lifetimes shown for the BA binary film. (b) Fitted lifetime values for isolated FRET dynamics as a function of approximate distance from the center to center of $n = 1$ and $n = 2$ layers within the mixed film.

Transient absorption measurements were repeated for the full range of A′ spacer cations, including neat donor, neat acceptor, and binary mixed films, in order to gain experimental understanding of FRET scaling in 2D PQW materials. The donor−acceptor distance, here defined as the center of a donor layer to the center of an acceptor layer, was determined from single-crystal diffraction as functions of each A′ site cation, and additional details regarding the determination of these distances can be found in the Supporting Information. For progressively longer spacer lengths of 16.4, 19.4, and 21.9 Å, respectively, FRET lifetimes of 14 ± 2, 29 ± 3, and 48 ± 3 ps were obtained from fitting donor-derived decays and are shown in Figure 3b. As such, FRET rates decrease with increasing distance for 2D PQWs in a nonlinear fashion as the electromagnetic coupling between the donor and acceptor decreases.

The observed trend in FRET lifetimes as a function of distance was compared to a computational model we developed to describe FRET in 2D materials. The model considers the PQWs as discrete three-dimensional slabs, where the radiative emission of the donor PQW is described by a classical oscillating dipole operating at its emission wavelength, λ_{PL} = 525 nm (see Figure 1b). The resulting electric fields in the materials are determined numerically using Comsol Multiphysics software. The geometrical configuration of this model, shown in Figure 4a, stacks three PQWs along the z direction with a $n = 1$ donor between two $n = 2$ acceptors. Importantly, they are separated by the distance d that accounts for the molecular spacers used in the experimental samples. The strength of the donor dipole is taken as μ = 2.5 eÅ, a value guided by a previous report.[43] We calculated the FRET rate by considering the electromagnetic absorption at the acceptor slabs in a system excited by a dipole situated at the center of the donor slab (see Figure 4a) using the expression[19,31]

$$k_{FRET} = \frac{2}{\hbar}\varepsilon_0 \mathrm{Im}[\varepsilon_A] \int_A |E|^2 dV \quad (1)$$

where ε_0 and ε_A are the permittivity of free space and the relative permittivity of the acceptor PQW, respectively. The volume integral of the electric field generated by the dipole inside the donor PQW is evaluated over the volume of the acceptor PQW, denoted as A, and surrounded by a dashed black line in Figure 4a. From this magnitude, we obtain

https://dx.doi.org/10.1021/jacs.0c12441
J. Am. Chem. Soc. XXXX, XXX, XXX−XXX

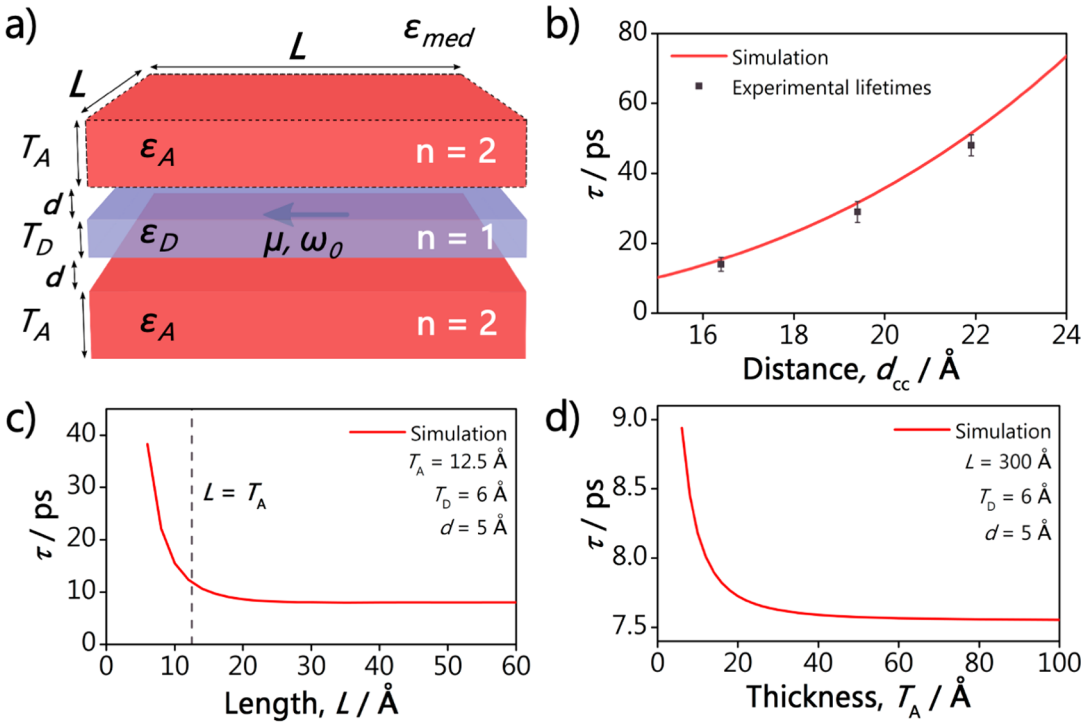

Figure 4. (a) Schematic diagram of the computational model for the system, along with the representation of its geometrical parameters. The system is composed of three stacked slabs with the $n = 1$ donor slab in the middle. The dashed lines surrounding the top $n = 2$ acceptor slab indicate the volume used for the integral in eq 1. (b) Comparison of the experimentally measured lifetimes with the values obtained from the simulated model. (c) Theoretical average lifetimes with respect to changes in the PQW length. The dashed line marks the value at which the length of the PQWs is the same as the acceptors' thickness; i.e., it becomes a cube. Above this value, the system rapidly reaches a stable value. (d) Theoretical average lifetimes with respect to changes in the acceptor PQW thickness.

theoretical lifetimes of the excited state in the donor PQW as $\tau = 1/k_{FRET}$. Lastly, we use a single-oscillator Lorentz model to define the permittivity of the slabs with parameters chosen to maintain consistency with previously reported dielectric constant values for similar materials.[44,45] In defining the dielectric constant this way, i.e., with shifted absorption lines between the $n = 1$ and $n = 2$ layers, we introduce information about the different strengths of quantum confinement in each subsystem. The permittivity of the simulated slabs is then given by

$$\varepsilon_r = \varepsilon_\infty + \frac{{\omega_p}^2}{{\omega_0}^2 - \omega^2 - 2i\omega\gamma} \quad (2)$$

In Figure 4b, we present theoretical results for the FRET lifetimes as we change the spacing d between the PQWs. The x-axis is presented in terms of center-to-center distance, d_{cc}, between the PQWs in order to offer a consistent description with the experimental data in Figure 3b, which is also included in this plot. We note that the experimental and theoretical data are in good agreement, indicating that the alkylammonium cations used in the experiment effectively behave as spacers and thus affect FRET rates. Furthermore, the data and model show FRET rates that rapidly decrease with increasing distance between the donor and acceptor. Fitting of these rates indicates that they scale with the center-to-center distance between the PQWs as approximately ${d_{cc}}^{-4}$, a trend observed in some reports involving 2D donor or acceptor states[17,20−23] but not observed for others.[26,27] Other factors, such as dielectric screening at the donor[26] and extended acceptor morphology,[19,27] can impact FRET rates and result in deviation from the expected trend for distance dependence in 2D systems.

The resulting FRET lifetimes we obtained through both the empirical and theoretical approaches are rapid, outpacing previously reported Auger recombination lifetimes of ∼80 ps in similar materials.[38,39] However, these FRET rates appear slower than in other binary and multiple mixed layer systems, such as those reported by Proppe et al.,[31] perhaps owing to the smaller donor−acceptor spectral overlap of the binary system studied herein. Given the same materials, sizes, and spacing, we would expect the FRET rates between $n = 2$ donors and $n = 3$ acceptors as well as consecutive sequences of larger layer n thicknesses to be higher as the result of the reduced difference between their electronic state shifts due to quantum confinement.

Our model goes beyond describing FRET between point-like dipoles in infinite 2D slabs. It also allows us to explore FRET for particular finite slab geometries that are subject to synthetic manipulation, such as lateral area control.[46] We calculated the impact of finite lateral area on the transfer time for a single FRET event. The numerical results of FRET lifetime versus PQW side length, L, are presented in Figure 4c for a donor−acceptor separation of $d = 0.5$ nm. We observe prompt convergence spanning from $\tau \approx 70$ ps at $L = 0.5$ nm to values approximately an order of magnitude lower, such as those observed in Figure 4b, when we consider values of $L > 2$ nm. At values of $L \leq d = 1.25$ nm, the system effectively approaches QD-like behavior rather than 2D quantum well characteristics. In this calculation, we neglect effects that the small lateral extent would suggest about lateral quantum confinement the particles may experience. From this data, we

https://dx.doi.org/10.1021/jacs.0c12441
J. Am. Chem. Soc. XXXX, XXX, XXX−XXX

conclude that, from the perspective of the geometrical coverage of donor PQWs by the acceptor ones, we should not expect changes in the typical time scale of a single FRET event with further increases in PQW area.

Given the rapid decay of the electric field of the classical oscillating dipole, the extension of the thickness of a PQW beyond the immediate proximity of the original excitation has a negligible effect on FRET rates given otherwise fixed acceptor properties, as seen in Figure 4d. However, although these data capture the dependency of the FRET rates on the spatial distribution of matter, they again do not specifically account for the effect of quantum confinement as a function of changing morphology. Nonetheless, from the combined evidence of Figure 4c,d, one could argue that the slab thicknesses depicted in Figure 4a and used to compute Figure 4b virtually maximize the FRET rate for a given spectral overlap as modeled by eq 1. In other words, from the perspective of this theoretical model, the PQW geometry observed in the experimental samples provides almost maximal FRET transfer rates for a given material pairing and interlayer distance, and neither extending the layer length nor stacking additional $n = 2$ acceptor layers should substantially alter FRET rates. Additional results of the theoretical model with respect to other parameters, such as dipole strengths and relative orientations, are included in the Supporting Information.

CONCLUSION

The controlled variation of the A′ site cations in $n = 1$ and $n = 2$ phases of 2D PQWs was successfully implemented as a nanoscopic tool for modifying electronic energy migration with respect to distance between donor and acceptor states with two-dimensional spatial extent. Having prepared binary, controlled mixtures for the examination of the scaling of FRET with distance, we obtained donor-derived lifetimes of 14, 29, and 48 ps for distances of 16.4, 19.4, and 21.9 Å, respectively. Computationally derived lifetimes for FRET are in agreement with empirical data for 2D PQWs, indicating FRET lifetimes that scale with distance as d_{cc}^{-4} for PQWs presenting a large lateral extent and moderate spectral overlap between donor and acceptor states. Importantly, overcoming the synthetic challenges posed in the pursuit of the controlled donor and acceptor mixtures of higher n layers for FRET studies will prove beneficial for ongoing and future studies of applications in which films are implemented. In that way, the extension of the empirical model for scaling FRET with distance could include consecutively longer alkylammonium cations that would increase the distance between layers. Overall, the synthetic and spectroscopic methods employed in this work for obtaining phase-pure and mixed-phase 2D PQW film and resultant ultrafast dynamics of FRET afford extensive control for factors that affect electronic processes, thus showing improved understanding of charge carrier behavior. Such understanding and vetted modeling opens possibilities for fast, even multiexcitonic FRET manipulations on ultrafast time scales through the implementation of 2D materials.

EXPERIMENTAL METHODS

Chemicals. Butylamine (99.5%), hexylamine (99%), octylamine (99%), hydroiodic acid (57 wt %, 99.95%), hypophosphorous acid (50 wt %), dimethylformamide (anhydrous), lead(II) oxide powder (≥99% trace metals basis), and methylamine hydrochloride (≥98%) were all purchased from Sigma-Aldrich. Ethyl ether (anhydrous) was purchased from Fisher Scientific. Methylamine hydrochloride was dried in an oven at 70 °C overnight before use. All other chemicals were used as received without further purification.

Crystal Syntheses..[40,41] *General Procedure for n = 1.* PbO powder (2232 mg, 10 mmol) was added to hydroiodic acid in a 50 mL Erlenmeyer flask and heated to boiling while stirring to afford a bright yellow solution. In a separate vial, the alkylamine was neutralized with 2 mL of hypophosphorous acid in an ice bath. The alkylammonium solution was then added to the reaction mixture. Orange precipitate initially crashed out but redissolved after additional heating. The reaction mixture was removed from heat and allowed to cool to room temperature to facilitate the precipitation of the crystalline product from the solution. The precipitate was separated from the reaction by vacuum filtration and washed with diethyl ether over a medium porosity fritted glass filter to afford orange, flake-like crystals. Crystals were stored in an evacuated desiccator until further use.

$(C_4H_9NH_3)_2PbI_4$. The general procedure for $n = 1$ was followed using butylamine (925 μL, 9.34 mmol) in 15 mL of hydroiodic acid.

$(C_6H_{13}NH_3)_2PbI_4$. The general procedure for $n = 1$ was followed using hexylamine (800 μL, 6.08 mmol) in 18 mL of hydroiodic acid.

$(C_8H_{17}NH_3)_2PbI_4$. The general procedure for $n = 1$ was followed using octylamine (700 μL, 4.24 mmol) in 20 mL of hydroiodic acid.

General Procedure for n = 2. PbO powder (2232 mg, 10 mmol) and methylamine hydrochloride were added to hydroiodic acid in a 50 mL Erlenmeyer flask and heated to boiling while stirring to afford a bright yellow solution. In a separate vial, the alkylamine was neutralized with 2 mL of hypophosphorous acid in an ice bath. The alkylammonium solution was then added to the reaction mixture and dissolved completely. The reaction mixture was removed from heat and allowed to slowly cool to room temperature to facilitate the precipitation of the crystalline product from the solution. The precipitate was separated from the reaction by vacuum filtration and washed with diethyl ether over a medium porosity fritted glass filter to afford red, flake-like crystals. Crystals were stored in an evacuated desiccator until further use.

$(C_4H_9NH_3)_2(CH_3NH_3)Pb_2I_7$. The general procedure for $n = 2$ was followed using butylamine (694 μL, 7 mmol), methylamine hydrochloride (338 mg, 5 mmol), and 15 mL of hydroiodic acid.

$(C_6H_{13}NH_3)_2(CH_3NH_3)Pb_2I_7$. The general procedure for $n = 2$ was followed using hexylamine (580 μL, 4.39 mmol), methylamine hydrochloride (338 mg, 5 mmol), and 18 mL of hydroiodic acid.

$(C_8H_{17}NH_3)_2(CH_3NH_3)Pb_2I_7$. The general procedure for $n = 2$ was followed using octylamine (165 μL, 1.02 mmol), methylamine hydrochloride (338 mg, 5 mmol), and 20 mL of hydroiodic acid.

Thin-Film Syntheses.[2] *General Procedure.* Amorphous glass substrates (2.5 cm × 2.5 cm × 1 mm) were cleaned 3× using deionized water followed by acetone and finally ethanol in a sonicated bath for 10 min. The substrates were then preteated for 10 min using an ultraviolet ozone (UVO) treatment method. Phase-pure $n = 1$ and $n = 2$ crystals were dissolved into 300 μL of dimethylformamide (DMF) in a nitrogen atmosphere. The glass substrate that was preheated to 110 °C was quickly transferred (1.5 s) to the spin-coating stage. Thirty μL of the solution was then immediately spin-coated onto the substrate and spun at 4000 rpm for 30 s. The resulting films were stored in a nitrogen atmosphere until further use. In the following, the films are denoted by the alkylammonium carbon chain length and the layer thickness; e.g., C4n1 refers to a film synthesized with butylammonium (four carbons) and of $n = 1$ phase and so forth.

C4n1. The general procedure for film synthesis was followed using 40 mg of $(C_4H_9NH_3)_2PbI_4$ dissolved into DMF.

C4n1 and C4n2 Mixture. The general procedure for film synthesis was followed using 20 mg of $(C_4H_9NH_3)_2PbI_4$ and 20 mg of $(C_4H_9NH_3)_2(CH_3NH_3)Pb_2I_7$ dissolved into DMF.

C4n2. The general procedure for film synthesis was followed using 40 mg of $(C_4H_9NH_3)_2(CH_3NH_3)Pb_2I_7$ dissolved into DMF.

C6n1. The general procedure for film synthesis was followed using 40 mg of $(C_6H_{13}NH_3)_2PbI_4$ dissolved into DMF.

https://dx.doi.org/10.1021/jacs.0c12441
J. Am. Chem. Soc. XXXX, XXX, XXX−XXX

C6n1 and C6n2 Mixture. The general procedure for film synthesis was followed using 20 mg of $(C_6H_{13}NH_3)_2PbI_4$ and 20 mg of $(C_6H_{13}NH_3)_2(CH_3NH_3)Pb_2I_7$ dissolved into DMF.

C6n2. The general procedure for film synthesis was followed using 40 mg of $(C_6H_{13}NH_3)_2(CH_3NH_3)Pb_2I_7$ dissolved into DMF.

C8n1. The general procedure for film synthesis was followed using 40 mg of $(C_8H_{17}NH_3)_2PbI_4$ dissolved in DMF.

C8n1 and C8n2 Mixture. The general procedure for film synthesis was followed using 20 mg of $(C_8H_{17}NH_3)_2PbI_4$ and 20 mg of $(C_8H_{17}NH_3)_2(CH_3NH_3)Pb_2I_7$ dissolved in DMF.

C8n2. The general procedure for film synthesis was followed using 40 mg of $(C_8H_{17}NH_3)_2(CH_3NH_3)Pb_2I_7$ dissolved into DMF.

X-ray Diffraction Measurements. Powder X-ray diffraction (PXRD) patterns were collected on a Rigaku Miniflex600 powder X-ray diffractometer (Cu Kα, λ = 1.5406 Å) operating at 40 kV/15 mA with a graphite monochromator and Kβ foil filter. Single-crystal X-ray diffraction was performed using a STOE IPDS II diffractometer (Mo Kα, λ = 0.71073 Å) operating at 50 kV/40 mA with a graphite monochromatizer.

Static Optical Measurements. Absorption spectra were measured using a Shimadzu 3600 UV−vis−NIR spectrophotometer. PL spectra were collected under 405 nm front-facing photoexcitation with a 35 fs pulse width laser diode.

Scanning Electron Microscopy. Scanning electron microscope images were acquired using a Hitachi SU4800-II cFEG SEM at an accelerating voltage of 2.0 kV. Materials were precoated with osmium using an SPI Osmium coater.

Transient Spectroscopy. Ultrafast experiments were performed using a Ti:sapphire amplifier with 2 kHz repetition rate and 35 fs pulse width. 400 nm pump pulses were generated using the frequency-doubled output of the laser with a BBO crystal. Time-resolved photoluminescence measurements were collected using a streak-camera with front-facing excitation. Photon counts were accumulated for 15 ms over 30 000 integrations. In transient absorption experiments, a small portion of the 800 nm Ti:sapphire output was focused into a sapphire crystal to produce white light probe pulses. 545 nm pump pulses were generated from the 800 nm laser output using an optical parametric amplifier (OPA). Probe pulses were mechanically time delayed using a translation stage and retroflector. Transient absorption spectra for each time point were averaged for 2 s, and then, three reproducible, separate scans were averaged together. Background subtraction and probe chirp correction were conducted for all raw spectra before data analysis. All spectroscopic studies were performed at room temperature and in ambient conditions.

■ ASSOCIATED CONTENT

Supporting Information

The Supporting Information is available free of charge at https://pubs.acs.org/doi/10.1021/jacs.0c12441.

Static structural and optical characterization of materials, additional transient absorption spectra, time-resolved photoluminescence experiments, a detailed explanation of the determination of the distances between quantum wells, and theoretical modelling (PDF)

■ AUTHOR INFORMATION

Corresponding Authors

Richard D. Schaller − *Department of Chemistry, Northwestern University, Evanston, Illinois 60208, United States; Center for Nanoscale Materials, Argonne National Laboratory, Lemont, Illinois 60439, United States;* orcid.org/0000-0001-9696-8830; Email: schaller@anl.gov

Mercouri G. Kanatzidis − *Department of Chemistry, Northwestern University, Evanston, Illinois 60208, United States; Material Science Division, Argonne National Laboratory, Lemont, Illinois 60439, United States;* orcid.org/0000-0003-2037-4168; Email: m-kanatzidis@northwestern.edu

Authors

Shobhana Panuganti − *Department of Chemistry, Northwestern University, Evanston, Illinois 60208, United States;* orcid.org/0000-0003-1762-527X

Lucas V. Besteiro − *Institut National de la Recherche Scientifique-Énergie, Matériaux et Télécommunications, Montreal, Quebec H5A 1K6, Canada;* orcid.org/0000-0001-7356-7719

Eugenia S. Vasileiadou − *Department of Chemistry, Northwestern University, Evanston, Illinois 60208, United States;* orcid.org/0000-0002-5714-9207

Justin M. Hoffman − *Department of Chemistry, Northwestern University, Evanston, Illinois 60208, United States;* orcid.org/0000-0003-1400-9180

Alexander O. Govorov − *Department of Physics and Astronomy, Ohio University, Athens, Ohio 45701, United States;* orcid.org/0000-0003-1316-6758

Stephen K. Gray − *Center for Nanoscale Materials, Argonne National Laboratory, Lemont, Illinois 60439, United States*

Complete contact information is available at: https://pubs.acs.org/10.1021/jacs.0c12441

Notes

The authors declare no competing financial interest.

■ ACKNOWLEDGMENTS

We acknowledge student support provided by the National Science Foundation under Grant No. DMREF-1629383. This material is based upon work supported by the National Science Foundation Graduate Research Fellowship Program under Grant No. DGE-1842165 (S.P.). At Northwestern University, this work was supported in part by grant SC0012541 from the US Department of Energy, Office of Science. This work was performed, in part, at the Center for Nanoscale Materials, a U.S. Department of Energy Office of Science User Facility, and supported by the U.S. Department of Energy, Office of Science, Office of Basic Energy Sciences, under Contract No. DE-AC02-06CH11357. This work made use of the EPIC facility of Northwestern University's NUANCE Center, which has received support from the SHyNE Resource (NSF ECCS-2025633), the IIN, and Northwestern's MRSEC program (NSF DMR-1720139).

■ REFERENCES

(1) Xia, F.; Wang, H.; Xiao, D.; Dubey, M.; Ramasubramaniam, A. Two-dimensional material nanophotonics. *Nat. Photonics* **2014**, *8* (12), 899−907.

(2) Tsai, H.; Nie, W.; Blancon, J.-C.; Stoumpos, C. C.; Asadpour, R.; Harutyunyan, B.; Neukirch, A. J.; Verduzco, R.; Crochet, J. J.; Tretiak, S.; Pedesseau, L.; Even, J.; Alam, M. A.; Gupta, G.; Lou, J.; Ajayan, P. M.; Bedzyk, M. J.; Kanatzidis, M. G.; Mohite, A. D. High-efficiency two-dimensional Ruddlesden−Popper perovskite solar cells. *Nature* **2016**, *536* (7616), 312−316.

(3) Das, S.; Pandey, D.; Thomas, J.; Roy, T. The Role of Graphene and Other 2D Materials in Solar Photovoltaics. *Adv. Mater.* **2019**, *31* (1), 1802722.

(4) Yu, X.; Sivula, K. Toward Large-Area Solar Energy Conversion with Semiconducting 2D Transition Metal Dichalcogenides. *ACS Energy Letters* **2016**, *1* (1), 315−322.

(5) Guzelturk, B.; Kelestemur, Y.; Olutas, M.; Delikanli, S.; Demir, H. V. Amplified Spontaneous Emission and Lasing in Colloidal Nanoplatelets. *ACS Nano* **2014**, *8* (7), 6599−6605.
(6) Kumar, S.; Jagielski, J.; Yakunin, S.; Rice, P.; Chiu, Y.-C.; Wang, M.; Nedelcu, G.; Kim, Y.; Lin, S.; Santos, E. J. G.; Kovalenko, M. V.; Shih, C.-J. Efficient Blue Electroluminescence Using Quantum-Confined Two-Dimensional Perovskites. *ACS Nano* **2016**, *10* (10), 9720−9729.
(7) Chen, Z.; Nadal, B.; Mahler, B.; Aubin, H.; Dubertret, B. Quasi-2D Colloidal Semiconductor Nanoplatelets for Narrow Electroluminescence. *Adv. Funct. Mater.* **2014**, *24* (3), 295−302.
(8) Smith, M. D.; Connor, B. A.; Karunadasa, H. I. Tuning the Luminescence of Layered Halide Perovskites. *Chem. Rev.* **2019**, *119* (5), 3104−3139.
(9) Ithurria, S.; Tessier, M. D.; Mahler, B.; Lobo, R. P. S. M.; Dubertret, B.; Efros, A. L. Colloidal nanoplatelets with two-dimensional electronic structure. *Nat. Mater.* **2011**, *10* (12), 936−941.
(10) Guzelturk, B.; Demir, H. V. Near-Field Energy Transfer Using Nanoemitters For Optoelectronics. *Adv. Funct. Mater.* **2016**, *26* (45), 8158−8177.
(11) Padgaonkar, S.; Olding, J. N.; Lauhon, L. J.; Hersam, M. C.; Weiss, E. A. Emergent Optoelectronic Properties of Mixed-Dimensional Heterojunctions. *Acc. Chem. Res.* **2020**, *53* (4), 763−772.
(12) Motti, S. G.; Crothers, T.; Yang, R.; Cao, Y.; Li, R.; Johnston, M. B.; Wang, J.; Herz, L. M. Heterogeneous Photon Recycling and Charge Diffusion Enhance Charge Transport in Quasi-2D Lead-Halide Perovskite Films. *Nano Lett.* **2019**, *19* (6), 3953−3960.
(13) Yuan, M.; Quan, L. N.; Comin, R.; Walters, G.; Sabatini, R.; Voznyy, O.; Hoogland, S.; Zhao, Y.; Beauregard, E. M.; Kanjanaboos, P.; Lu, Z.; Kim, D. H.; Sargent, E. H. Perovskite energy funnels for efficient light-emitting diodes. *Nat. Nanotechnol.* **2016**, *11* (10), 872−877.
(14) Santra, P. K.; Kamat, P. V. Tandem-Layered Quantum Dot Solar Cells: Tuning the Photovoltaic Response with Luminescent Ternary Cadmium Chalcogenides. *J. Am. Chem. Soc.* **2013**, *135* (2), 877−885.
(15) Menke, S. M.; Luhman, W. A.; Holmes, R. J. Tailored exciton diffusion in organic photovoltaic cells for enhanced power conversion efficiency. *Nat. Mater.* **2013**, *12* (2), 152−157.
(16) Förster, T. Intermolecular energy migration and fluorescence. In *Biological Physics*; Mielczarek, E. V., Greenbaum, E., Knox, R. S., Eds.; American Institute of Physics: New York, 1993; pp 148−160.
(17) Hernández-Martínez, P. L.; Govorov, A. O.; Demir, H. V. Generalized Theory of Förster-Type Nonradiative Energy Transfer in Nanostructures with Mixed Dimensionality. *J. Phys. Chem. C* **2013**, *117* (19), 10203−10212.
(18) Liu, X.; Qiu, J. Recent advances in energy transfer in bulk and nanoscale luminescent materials: from spectroscopy to applications. *Chem. Soc. Rev.* **2015**, *44* (23), 8714−8746.
(19) Rowland, C. E.; Fedin, I.; Zhang, H.; Gray, S. K.; Govorov, A. O.; Talapin, D. V.; Schaller, R. D. Picosecond energy transfer and multiexciton transfer outpaces Auger recombination in binary CdSe nanoplatelet solids. *Nat. Mater.* **2015**, *14*, 484.
(20) Erdem, O.; Gungor, K.; Guzelturk, B.; Tanriover, I.; Sak, M.; Olutas, M.; Dede, D.; Kelestemur, Y.; Demir, H. V. Orientation-Controlled Nonradiative Energy Transfer to Colloidal Nanoplatelets: Engineering Dipole Orientation Factor. *Nano Lett.* **2019**, *19* (7), 4297−4305.
(21) Loiudice, A.; Saris, S.; Buonsanti, R. Tunable Metal Oxide Shell as a Spacer to Study Energy Transfer in Semiconductor Nanocrystals. *J. Phys. Chem. Lett.* **2020**, *11*, 3430−3435.
(22) Gaudreau, L.; Tielrooij, K. J.; Prawiroatmodjo, G. E. D. K.; Osmond, J.; de Abajo, F. J. G.; Koppens, F. H. L. Universal Distance-Scaling of Nonradiative Energy Transfer to Graphene. *Nano Lett.* **2013**, *13* (5), 2030−2035.
(23) Swathi, R. S.; Sebastian, K. L. Resonance energy transfer from a dye molecule to graphene. *J. Chem. Phys.* **2008**, *129* (5), No. 054703.
(24) Ajayi, O. A.; Anderson, N. C.; Cotlet, M.; Petrone, N.; Gu, T.; Wolcott, A.; Gesuele, F.; Hone, J.; Owen, J. S.; Wong, C. W. Time-resolved energy transfer from single chloride-terminated nanocrystals to graphene. *Appl. Phys. Lett.* **2014**, *104* (17), 171101.
(25) Raja, A.; Montoya-Castillo, A.; Zultak, J.; Zhang, X.-X.; Ye, Z.; Roquelet, C.; Chenet, D. A.; van der Zande, A. M.; Huang, P.; Jockusch, S.; Hone, J.; Reichman, D. R.; Brus, L. E.; Heinz, T. F. Energy Transfer from Quantum Dots to Graphene and MoS2: The Role of Absorption and Screening in Two-Dimensional Materials. *Nano Lett.* **2016**, *16* (4), 2328−2333.
(26) Taghipour, N.; Hernandez Martinez, P. L.; Ozden, A.; Olutas, M.; Dede, D.; Gungor, K.; Erdem, O.; Perkgoz, N. K.; Demir, H. V. Near-Unity Efficiency Energy Transfer from Colloidal Semiconductor Quantum Wells of CdSe/CdS Nanoplatelets to a Monolayer of MoS2. *ACS Nano* **2018**, *12* (8), 8547−8554.
(27) Prins, F.; Goodman, A. J.; Tisdale, W. A. Reduced Dielectric Screening and Enhanced Energy Transfer in Single- and Few-Layer MoS2. *Nano Lett.* **2014**, *14* (11), 6087−6091.
(28) Liu, H.; Wang, T.; Wang, C.; Liu, D.; Luo, J. Exciton Radiative Recombination Dynamics and Nonradiative Energy Transfer in Two-Dimensional Transition-Metal Dichalcogenides. *J. Phys. Chem. C* **2019**, *123* (15), 10087−10093.
(29) Hong, X.; Ishihara, T.; Nurmikko, A. V. Dielectric confinement effect on excitons in PbI4-based layered semiconductors. *Phys. Rev. B: Condens. Matter Mater. Phys.* **1992**, *45* (12), 6961−6964.
(30) Lei, L.; Seyitliyev, D.; Stuard, S.; Mendes, J.; Dong, Q.; Fu, X.; Chen, Y.-A.; He, S.; Yi, X.; Zhu, L.; Chang, C.-H.; Ade, H.; Gundogdu, K. So, F., Efficient Energy Funneling in Quasi-2D Perovskites: From Light Emission to Lasing. *Adv. Mater.* **2020**, *32* (16), 1906571.
(31) Proppe, A. H.; Elkins, M. H.; Voznyy, O.; Pensack, R. D.; Zapata, F.; Besteiro, L. V.; Quan, L. N.; Quintero-Bermudez, R.; Todorovic, P.; Kelley, S. O.; Govorov, A. O.; Gray, S. K.; Infante, I.; Sargent, E. H.; Scholes, G. D. Spectrally Resolved Ultrafast Exciton Transfer in Mixed Perovskite Quantum Wells. *J. Phys. Chem. Lett.* **2019**, *10* (3), 419−426.
(32) Williams, O. F.; Guo, Z.; Hu, J.; Yan, L.; You, W.; Moran, A. M. Energy transfer mechanisms in layered 2D perovskites. *J. Chem. Phys.* **2018**, *148* (13), 134706.
(33) Zheng, K.; Chen, Y.; Sun, Y.; Chen, J.; Chábera, P.; Schaller, R.; Al-Marri, M. J.; Canton, S. E.; Liang, Z.; Pullerits, T. Inter-phase charge and energy transfer in Ruddlesden−Popper 2D perovskites: critical role of the spacing cations. *J. Mater. Chem. A* **2018**, *6* (15), 6244−6250.
(34) Singldinger, A.; Gramlich, M.; Gruber, C.; Lampe, C.; Urban, A. S. Nonradiative Energy Transfer between Thickness-Controlled Halide Perovskite Nanoplatelets. *ACS Energy Letters* **2020**, *5* (5), 1380−1385.
(35) Peng, S.; Wei, Q.; Wang, B.; Zhang, Z.; Yang, H.; Pang, G.; Wang, K.; Xing, G.; Sun, X. W.; Tang, Z. Suppressing Strong Exciton−Phonon Coupling in Blue Perovskite Nanoplatelet Solids by Binary Systems. *Angew. Chem., Int. Ed.* **2020**, *59* (49), 22156−22162.
(36) Dahlman, C. J.; DeCrescent, R. A.; Venkatesan, N. R.; Kennard, R. M.; Wu, G.; Everest, M. A.; Schuller, J. A.; Chabinyc, M. L. Controlling Solvate Intermediate Growth for Phase-Pure Organic Lead Iodide Ruddlesden−Popper (C4H9NH3)2(CH3NH3)n−1PbnI3n+1 Perovskite Thin Films. *Chem. Mater.* **2019**, *31* (15), 5832−5844.
(37) Li, T.; Zeidell, A. M.; Findik, G.; Dunlap-Shohl, W. A.; Euvrard, J.; Gundogdu, K.; Jurchescu, O. D.; Mitzi, D. B. Phase-Pure Hybrid Layered Lead Iodide Perovskite Films Based on a Two-Step Melt-Processing Approach. *Chem. Mater.* **2019**, *31* (11), 4267−4274.
(38) Fang, H.-H.; Yang, J.; Adjokatse, S.; Tekelenburg, E.; Kamminga, M. E.; Duim, H.; Ye, J.; Blake, G. R.; Even, J.; Loi, M. A. Band-Edge Exciton Fine Structure and Exciton Recombination Dynamics in Single Crystals of Layered Hybrid Perovskites. *Adv. Funct. Mater.* **2020**, *30* (6), 1907979.
(39) Liang, Y.; Shang, Q.; Wei, Q.; Zhao, L.; Liu, Z.; Shi, J.; Zhong, Y.; Chen, J.; Gao, Y.; Li, M.; Liu, X.; Xing, G.; Zhang, Q. Lasing from

https://dx.doi.org/10.1021/jacs.0c12441
J. Am. Chem. Soc. XXXX, XXX, XXX−XXX

Mechanically Exfoliated 2D Homologous Ruddlesden−Popper Perovskite Engineered by Inorganic Layer Thickness. *Adv. Mater.* **2019**, *31* (39), 1903030.
(40) Stoumpos, C. C.; Cao, D. H.; Clark, D. J.; Young, J.; Rondinelli, J. M.; Jang, J. I.; Hupp, J. T.; Kanatzidis, M. G. Ruddlesden−Popper Hybrid Lead Iodide Perovskite 2D Homologous Semiconductors. *Chem. Mater.* **2016**, *28* (8), 2852−2867.
(41) Spanopoulos, I.; Hadar, I.; Ke, W.; Tu, Q.; Chen, M.; Tsai, H.; He, Y.; Shekhawat, G.; Dravid, V. P.; Wasielewski, M. R.; Mohite, A. D.; Stoumpos, C. C.; Kanatzidis, M. G. Uniaxial Expansion of the 2D Ruddlesden−Popper Perovskite Family for Improved Environmental Stability. *J. Am. Chem. Soc.* **2019**, *141* (13), 5518−5534.
(42) Yang, Y.; Yang, M.; Zhu, K.; Johnson, J. C.; Berry, J. J.; van de Lagemaat, J.; Beard, M. C. Large polarization-dependent exciton optical Stark effect in lead iodide perovskites. *Nat. Commun.* **2016**, *7* (1), 12613.
(43) Proppe, A. H.; Walters, G. W.; Alsalloum, A. Y.; Zhumekenov, A. A.; Mosconi, E.; Kelley, S. O.; De Angelis, F.; Adamska, L.; Umari, P.; Bakr, O. M.; Sargent, E. H. Transition Dipole Moments of n = 1, 2, and 3 Perovskite Quantum Wells from the Optical Stark Effect and Many-Body Perturbation Theory. *J. Phys. Chem. Lett.* **2020**, *11* (3), 716−723.
(44) Phillips, L. J.; Rashed, A. M.; Treharne, R. E.; Kay, J.; Yates, P.; Mitrovic, I. Z.; Weerakkody, A.; Hall, S.; Durose, K. Dispersion relation data for methylammonium lead triiodide perovskite deposited on a (100) silicon wafer using a two-step vapour-phase reaction process. *Data in Brief* **2015**, *5*, 926−928.
(45) Blancon, J. C.; Stier, A. V.; Tsai, H.; Nie, W.; Stoumpos, C. C.; Traoré, B.; Pedesseau, L.; Kepenekian, M.; Katsutani, F.; Noe, G. T.; Kono, J.; Tretiak, S.; Crooker, S. A.; Katan, C.; Kanatzidis, M. G.; Crochet, J. J.; Even, J.; Mohite, A. D. Scaling law for excitons in 2D perovskite quantum wells. *Nat. Commun.* **2018**, *9* (1), 2254.
(46) She, C.; Fedin, I.; Dolzhnikov, D. S.; Dahlberg, P. D.; Engel, G. S.; Schaller, R. D.; Talapin, D. V. Red, Yellow, Green, and Blue Amplified Spontaneous Emission and Lasing Using Colloidal CdSe Nanoplatelets. *ACS Nano* **2015**, *9* (10), 9475−9485.

https://dx.doi.org/10.1021/jacs.0c12441
J. Am. Chem. Soc. XXXX, XXX, XXX−XXX